

Wasserstein distance based semi-supervised manifold learning and application to GNSS multi-path detection

Antoine Blais ^{*1} and Nicolas Couëllan ^{†1,2}

¹ENAC, Université de Toulouse, 7 Avenue Édouard Belin,
BP 54005, 31055 Toulouse Cedex 4, France

²Institut de Mathématiques de Toulouse, Université de Toulouse,
UPS IMT, F-31062 Toulouse Cedex 9, France

December 8, 2025

Abstract

The main objective of this study is to propose an optimal transport based semi-supervised approach to learn from scarce labelled image data using deep convolutional networks. The principle lies in implicit graph-based transductive semi-supervised learning where the similarity metric between image samples is the Wasserstein distance. This metric is used in the label propagation mechanism during learning. We apply and demonstrate the effectiveness of the method on a Global Navigation Satellite System (GNSS) real life application. More specifically, we address the problem of multi-path interference detection. Experiments are conducted under various signal conditions. The results show that for specific choices of hyperparameters controlling the amount of semi-supervision and the level of sensitivity to the metric, the classification accuracy can be significantly improved over the fully supervised training method.

Keywords— Convolutional neural network, GNSS, multi-path detection, semi-supervised learning, Wasserstein distance, Earth mover Distance.

1 Introduction

Many engineering application contexts could take advantage of recent and successful developments of artificial intelligence. However, it is often difficult to gather a sufficiently large set of labelled samples to train models

^{*}Corresponding author: antoine.blais@recherche.enac.fr

[†]nicolas.couellan@recherche.enac.fr

such as deep learning architectures. This is particularly true for Convolutional Neural Network (CNN) based algorithms characterised by a large amount of convolutional blocks containing numerous filters. Indeed, the more complex the architecture, the more parameters there are to be trained, requiring therefore more labelled data.

The principle of Semi-Supervised Learning (SSL) has been introduced to handle situations where large amount of data is available but only few samples are labelled [Chapelle et al., 2006, Engelen and Hoos, 2019, Chen et al., 2024]. There are two main categories of SSL techniques. First, inductive methods such as wrappers method [Zhu, 2008] or co-training methods [Blum and Mitchell, 1998, Xu et al., 2013] have been proposed. They construct pseudo-labels using a pretrained supervised learning procedure and require usually a second training phase with the pseudo-labels. When a similarity measure between samples is available, the second class of techniques known as transductive methods can also be employed [Weston et al., 2012]. The graph-based methods are popular approaches along this line. They rely on the reasonable assumption that in practice data lie on a low dimensional smooth manifold [Chapelle et al., 2006]. In other words, it assumes that when data are similar their labels should be similar. The similarity metric between data allows the construction of an explicit or implicit graph between the samples. In graph-based transductive SSL methods, the aim is to train a model on both labelled and unlabelled data through a label inheritance mechanism between similar samples, also known as label propagation.

When dealing with image input samples, it has been shown that the Earth Mover’s Distance (EMD) and more generally the Wasserstein distance [Friesecke, 2025] is a relevant similarity measure that matches perceptual similarity better than other distances commonly used in image processing [Rubner et al., 2000]. Therefore, the availability of an efficient similarity measure for image samples advocates for the use of a graph-based SSL approach to train deep learning models when labelled images are scarce. SSL has been proposed in the past in the context of neural networks [Weston et al., 2012] and the Wasserstein distance has been utilized in other deep learning contexts such as Wasserstein GAN [Arjovsky et al., 2017] or Wasserstein distance based deep adversarial transfer learning [Cheng et al., 2020]. However, to the best of our knowledge, it has not been proposed for a real life application involving semi-supervised CNN in the literature. The aim of this study is to show that using a similarity measure based on optimal transport, image classification with few labelled samples can be significantly improved using SSL. The real life application we consider is the detection of interference in GNSS signals. The signals are shaped as multi-channel images where the similarity measure between signals is defined as the Wasserstein distance metric. The detection of multi-path interference is of great importance for GNSS as their presence can greatly alter the estimated position of the receiver. When receivers are embedded in systems such as aircraft, providing efficient and robust GNSS is critical.

The main contribution of this study is the original combination of SSL and CNN using the Wasserstein distance metric. More specifically, to the best of our knowledge this is one of the first study demonstrating a

successful implementation of such ideas to improve predicting performance of a CNN through SSL. Additionally, our implementation preserves the decomposition structure of the SSL regularised training loss in order to process large unlabelled data sets by batches of data and can then benefit from stochastic gradient based techniques during training. Furthermore, the use of optimal transport to evaluate the similarity between GNSS signals has never been proposed before. This work also shows that in GNSS applications where limited labelled data are available, one can use the regularity assumption to train Machine Learning (ML) models. Least but not last, this is a step towards data frugality in deep learning.

The rest of this article is structured as follows. First, section 2 clarifies the principle of SSL and the underlying concept of smoothness enforcing regularization. Then, the GNSS application is presented in section 3. At the same time, the distance metric chosen for semi-supervised training is exposed as it is data dependant. Section 4 details afterwards the test bench and the experiments which have been set up to assess the performance of SSL in the context of GNSS multi-path detection. Next, results are presented and thoroughly discussed in section 5. Finally, section 6 concludes the article.

2 Semi-supervised learning

In this section, we introduce the general model that makes use of general data hypothesis in order to learn from unlabelled data. Next, we specify the choices we propose to construct the numerical model and explain the computation of distances between data samples.

2.1 General semi-supervised framework

When learning from data, several underlying assumptions are commonly admitted [Chapelle et al., 2006]. The *manifold hypothesis* is a basic assumption in most machine learning problems. It states that the high dimensional data must lie in low dimensional manifold thus avoiding the curse of dimensionality when designing learning algorithms. The *smoothness assumption* is also commonly admitted and is of great importance in the model we consider. It assumes that the label function of the data varies smoothly with the distance between samples and even more so when in high density regions of the data space.

Consider a neural network $f(x, \theta)$ where $x \in \mathcal{D} := \mathcal{D}_S \cup \mathcal{D}_U$ where \mathcal{D}_S is the set of all labelled samples (later \mathcal{Y} will denote the corresponding set of labels), \mathcal{D}_U is the set of unlabelled samples, and θ are the neural network parameters (weights and biases). As in [Weston et al., 2012], the above smoothness assumption may be used as a regularizer in the empirical risk minimization training problem in order to train the neural network. More specifically, the following composite loss function may be constructed:

$$\min_{\theta} \sum_{(x,y) \in \mathcal{D}_S \times \mathcal{Y}} \mathcal{L}_S(y, f(x, \theta)) + \lambda \sum_{(x,x') \in \mathcal{D} \times \mathcal{D}} \mathcal{L}_U(f(x, \theta), f(x', \theta)) \quad (1)$$

where \mathcal{L}_S and \mathcal{L}_U are respectively loss and regularization functions for supervised and unsupervised learning respectively, $y \in \mathcal{Y}$ are the labels, and λ is a hyperparameter that controls the trade-off between supervision \mathcal{L}_S and the smoothness enforcing regularization \mathcal{L}_U . The loss \mathcal{L}_S may be any suitable error function for the learning problem at hand that calculates discrepancies between label and model prediction (ex: Mean squared error, Mean absolute error, binary cross-entropy,...). To choose \mathcal{L}_U , several strategies have been proposed [Weston et al., 2012]. Our choice will be explained next.

2.2 Smoothness enforcing regularization

To enforce smoothness of the model so that unlabelled data can inherit information from labelled neighbours, we propose to carry out label propagation through the model [Chapelle et al., 2006]. The idea is to calculate model predictions for pairs of data samples and weight the corresponding squared difference between the pair of predictions by their corresponding relative distance in the input space. The choice of distance metric in the input space to decide whether input samples are neighbours or not is specific to the nature of data and will be addressed later in Section 3.2. More specifically, our choice for \mathcal{L}_U is defined as follows: consider that $\{1, \dots, L\}$ contains the indices of labelled input samples and $\{L+1, \dots, L+U\}$ contains the indices of unlabelled input samples (with usually $U \gg L$), we define the total smoothing regularization as

$$\sum_{\substack{i,j=1 \\ (i \leq L) \oplus (j \leq L)}}^{L+U} \mathcal{L}_U(f(x_i, \theta), f(x_j, \theta)) \quad (2)$$

with

$$\mathcal{L}_U(f(x_i, \theta), f(x_j, \theta)) = W_{ij} \|f(x_i, \theta) - f(x_j, \theta)\|^2 \quad (3)$$

and where $W_{ij} \in [0, 1]$ is a weight parameter that is close to 1 if the distance between x_i and x_j is small and near 0 otherwise. In other words, W_{ij} controls the similarity between x_i and x_j and is computed through the Gaussian kernel similarity measure as follows [Belkin and Niyogi, 2003]:

$$W_{ij} = \exp \left\{ -\frac{d(x_i, x_j)^2}{\sigma} \right\} \quad (4)$$

where $d(x_i, x_j)$ is the distance metric between the samples x_i and x_j (see Section 3.2) and σ is a bandwidth parameter to control the sensitivity of W_{ij} to the similarity within the sample pair. Observe that in (2), the sum over i and j is taken over all pairs of samples once and that the operator \oplus indicates that a pair where both samples have labels is excluded from the sum. This specific handling of pairs of samples ensures that we are not computing any smoothing term when both samples have labels as this might be a conflicting objective for two samples that have distinct labels. Indeed, this mechanism gives more importance to ground truth through the \mathcal{L}_S error term rather than relying on the smoothness assumption.

When training the neural network with a stochastic optimization algorithm such as stochastic gradient descent (SGD) or its variants (ex: ADAM,

ADAGRAD and other) [Wright and Recht, 2022, Kingma and Ba, 2017], it is important that the loss function remains separable with respect to samples. Note that the way we define \mathcal{L}_U preserves this separability and it is possible to construct mini-batches where only pairs of samples within the mini-batch are considered during the iterative process. Therefore the proposed procedure also scales up to large data sets.

3 GNSS application

In this section, we first describe the data used to assess the combination of CNN and SSL. The objective to detect samples contaminated by multi-path signals is also clarified. Then, the definition of the Wasserstein distance metric selected to effectively put into practice semi-supervised learning is given. The strength of this particular metric to perform image classification in our context is explained as well.

3.1 GNSS Image data set

The data of interest in this study are produced by the Radio Frequency (RF) front-end of a GNSS receiver. More precisely, the signal available at the output of the RF front-end comes in two orthogonal channels. It is then shaped into two 2-Dimensional (2-D) matrices or equivalently a pair of images [Blais et al., 2022], [González et al., 2024]. The components of the pair are noted I and Q by convention in the GNSS community. Figure 1(a) displays an example of a pair of images. Figure 9(a) in Appendix A offers an equivalent 3-Dimensional (3-D) representation. Each pair of images is a snapshot of the received signal at a given time, a mix of the signal of interest, of the receiver noise and of any other disturbing interference captured by the antenna. A pair of images could be seen by analogy as the stereoscopic vision of a scene from a 3-D movie provided by polarized glasses.

This image representation has proven to be efficient when coupled to a CNN to detect a multi-path, or echo, signal affecting the Line-Of-Sight (LOS) signal [Blais et al., 2022]. It has also been demonstrated that the same association was effective to estimate the parameters of the multi-path signal [González et al., 2024]. The CNN implemented in the publications mentioned above need large amount of labelled data to be trained. However, real labelled data are scarce or expensive in the GNSS field. Then, a synthetic data generator has been used to create training and testing data sets. In this study, the synthetic data generator [Blais et al., 2025b] is also used but the purpose is to show that it is possible to reduce the dependency to the generator by using semi-supervised learning. The objective is to analyze whether the performance in detecting multi-path contamination of the signal of interest is improved or not by introducing unlabelled data in the learning process. The source code of the synthetic data generator is freely available under the terms of the GNU General Public License (GPL) version 3 license.

The original resolution of the images produced by the generator is 89x81 for physical compliance with the receiver hardware and signal pro-

cessing requirements. However, previous research works have shown that a reduction in resolution to as low as 26×26 still gives high detection accuracy for a much lower training time and computing power. Hence, this resolution has been retained for this study.

Images are always composed of at least the LOS signal and of the receiver noise. The LOS signal is modelled as depicted in Figure 1(b) or equivalently in Figure 9(b). The noise is considered to be an independent additive Gaussian random variable. The ratio between the signal and the noise power levels is set by the C/N_0 value, a classic figure of merit for quality of reception in GNSS receivers. In addition may come a multi-path distortion parameterized by its deviation in amplitude, time, frequency and phase with respect to the LOS signal. The model of the multi-path distortion is hence the same as for the LOS signal drawn in Figures 1(b) or 9(b) but attenuated in amplitude, shifted in time and frequency, and rotated in phase between I and Q . The probability density functions and ranges of the parameters are detailed in [González et al., 2024]. Figures 1(c) and 9(c) represent a multi-path signal characterized by a specific phase rotation of 90° which causes a swap between picture I and picture Q as they are orthogonal representations of the signal. The aggregation of the LOS signal and of the multi-path interference is pictured in Figures 1(d) and 9(d). Finally, Figures 1(a) and 9(a) are an example of a pair of full composite images produced by the generator. It is the addition of noise to the aggregation of the LOS signal and of the multi-path interference represented in Figures 1(c) and 9(c).

Each pair of images is labelled with a θ if it is distortion-free or with a 1 if it is polluted by a multi-path signal.

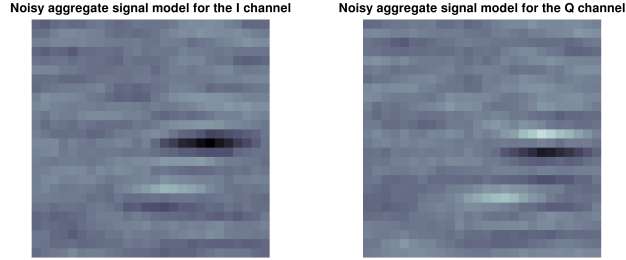
3.2 Wasserstein distance metric for multi-path detection

The input data for multi-path detection are composed of 2-D phased images spread on two channels (I and Q) and could be seen as images in the complex space, meaning that each pixel of an image has a complex value (I corresponding to the real part and Q the imaginary part). As recalled below, an efficient metric to compare two images is to consider the Wasserstein distance that computes the minimum energy cost to map one image seen as a probability distribution to the other image.

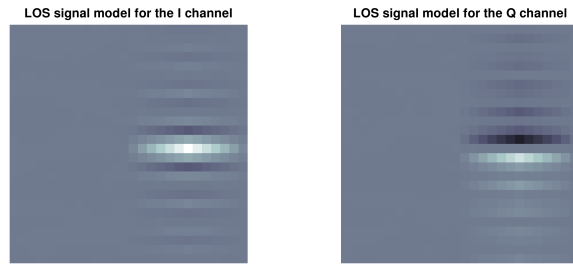
However, to the best of our knowledge, there is no computational procedure to compute this metric when images are seen as complex measures. For this reason, we propose to compute the Wasserstein distance between two pairs (I, Q) and (I', Q') of images by independently computing the optimal transportation cost between the pair (I, I') first and then (Q, Q') . The sum of the two optimal transportation costs will then be considered as the distance between the two pairs (I, Q) and (I', Q') of images.

The Wasserstein distance as an optimisation problem

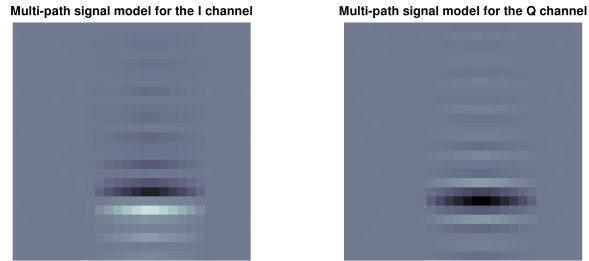
The underlying theoretical framework for computing the Wasserstein distance between two images a and b is the Monge–Kantorovitch optimal transport problem [Peyré and Cuturi, 2019, Friecke, 2025]. Consider



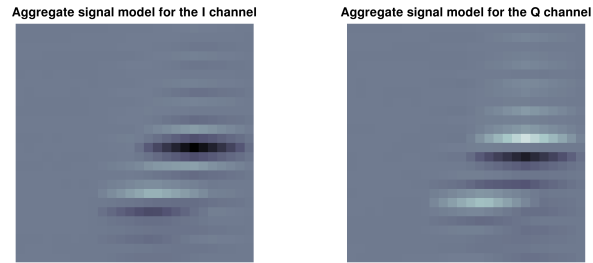
(a) Full image



(b) Direct signal model



(c) Multi-path signal model



(d) Aggregate signal model

Figure 1: Examples of pairs of I and Q images from the data generator.

$\{a_i\}$ for $i \in \{1, \dots, n\}$ and $\{b_j\}$ for $j \in \{1, \dots, m\}$ the pixel values of a and b respectively. Assume also that the images are offset and scaled so that $a_i \geq 0$ and $\sum_i a_i = 1$ and $b_j \geq 0$ and $\sum_j b_j = 1$ so that they can be seen as discrete probability distributions. In that case, the Wasserstein distance is the minimum energy required to transport image a to image b and can be formulated as the optimal objective value of the following optimization problem:

$$\begin{aligned} \min_{P \in [0,1]^{n \times m}} \quad & \sum_{i=1}^n \sum_{j=1}^m P_{ij} C_{ij} \\ \text{with respect to} \quad & \sum_{j=1}^m P_{ij} = a_i \quad \forall i = 1, \dots, n, \\ & \sum_{i=1}^n P_{ij} = b_j \quad \forall j = 1, \dots, m. \end{aligned}$$

where P is the unknown mass transportation matrix and C the given matrix of Euclidean distances between pixels.

The first set of constraints for each i corresponds to the conservation of the mass of image a during transport while the second set of constraints for each j represents the conservation of the mass received in image b . The above optimization problem is a linear programming problem and can be efficiently solved even for large dimensional images. This computation will be carried out for each pair of image (I, I') or (Q, Q') in the GNSS application.

Note on the computation of the pixel distance matrix C : the Euclidean distance between pixels involved in the above optimization problem is not sample dependent and can be computed once and applied during the whole iterative calculation process of the Wasserstein distance. To do so, images are first flattened using a flattening function $flatten : \mathcal{R}^n \times \mathcal{R}^n \rightarrow \mathcal{R}^{n^2} : (k, l) \rightarrow l + (k-1)n$, then the Euclidean distance between the pixels (p, q) and (k, l) of two images is given by $C_{ij} = \sqrt{(p-k)^2 + (q-l)^2}$ where $i = flatten(p, q)$ and $j = flatten(k, l)$.

4 Experiments

In this section, our SSL experimental framework is detailed. Firstly, the CNN architecture is displayed. Then, the data sets are exposed in depth. Lastly, the methodology of the experiments is explained.

4.1 CNN architecture

The CNN architecture implemented in this work is depicted in Figure 2. It is part of the Visual Geometry Group (VGG) network class [Simonyan and Zisserman, 2015]. This kind of neural network has been obsoleted for long by other structures such as ResNet [He et al., 2016], Inception [Szegedy et al., 2016] or DenseNet [Huang et al., 2018]. However,

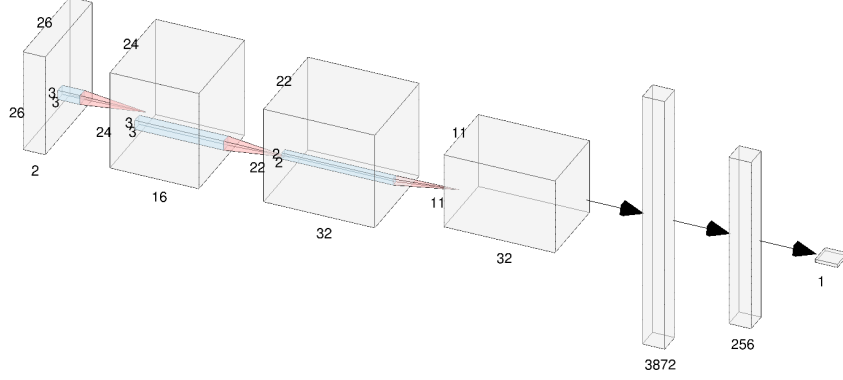


Figure 2: Architecture of the CNN used in this work [LeNail, 2019].

our approach in this study is to emphasise the methodological aspects of the SSL technique rather than detail a fully optimised neural architecture framework. For this reason, we have chosen to use a baseline neural network architecture (the VGG architecture) that is commonly accepted as efficient in a wide range of applications on images. Using alternative architectures the proposed method would be exactly identical as the one detailed in this article. The model performance could even achieve better results as an optimal neural architecture could be found for the application at hand. However, this would not highlight the role of SSL but rather the optimisation of the architecture. The choice of architecture is therefore secondary and this is why in the sequel of the article we will only consider a VGG-like neural network.

The input tensor made of a pair of 26×26 dimensional I and Q images is first analysed by a set of 16 filters of dimension 3×3 . Next, another set of 32 filters of dimension 3×3 is applied, followed by a 2×2 dimensional max pooling layer which completes the convolutional part of the network. The data are then flattened to feed a 3872 neurons linear layer. A layer of 256 neurons with a Rectified Linear Unit (RELU) activation function takes over to feed the final output neuron which makes use of a sigmoid activation function.

The CNN code has been written in the Python language using the PyTorch library [Paszke et al., 2019]. More specifically, the key function `ot.lp.emd` of the Python Optimal Transport (POT) library [Flamary et al., 2024] has been used to calculate the Wasserstein distance between pair of images. Again, the CNN code [Blais et al., 2025a] is freely available under the terms of the GNU GPL version 3 license.

4.2 Data sets composition

The data sets used for training and validation were elaborated in accordance with the GNSS context as well as with our SSL assessment objective. At the highest level, three C/N_0 ratios have been considered

to address realistic operating conditions of a GNSS receiver:

- 37 dBHz, corresponding to rather poor receiving conditions,
- 40 dBHz, which could be interpreted as a mid-range value,
- 43 dBHz, reflecting fairly good receiving conditions.

Then, for each C/N_0 ratio the distribution between labelled and unlabelled samples was made as follows for training:

- The total number of samples was set to 200. This is the sum of the number of labelled samples N_{SUP} and of the number of unlabelled samples N_{UNSUP} . It will be shown in section 5.1 that at $N_{\text{SUP}} = 200$ the classification accuracy is not growing significantly anymore and no appreciable learning gain is expected for greater N_{SUP} .
- The values of N_{SUP} have been staggered in the set $\{25, 40, 50, 60, 75\}$. Again, it will be emphasized in section 5.1 that below $N_{\text{SUP}} = 25$ training is unreliable while above $N_{\text{SUP}} = 75$ we are in situations where the majority of samples are labelled and these use cases are out of the scope of this study.

For the validation step, the number of samples, labelled by definition, was systematically set to 100.

Finally, the training and validation data sets were balanced with respect to the number of samples disturbed by a multi-path or not. The parameters of the multi-path, amplitude, time, frequency and phase, are not detailed here but they are presented in detail in [González et al., 2024]. They were also set to reflect realistic receiving conditions encountered by a GNSS receiver.

4.3 Methodology

In order to establish the performance of SSL, for each measurement point the following procedure was applied for training and validation of the network:

- 299 runs were executed. A run is one learning experience, starting from random initialisation of the weights of the network to the convergence of the loss function close to zero.
- 55 epochs have been carried out in each run. An epoch is defined as the complete scan of the training data set. This value of 55 was high enough to ensure the convergence of the loss function,
- At the end of each epoch a validation step was carried out, calculating the accuracy over the full validation data set.

More specifically about training, it is also worth noting that \mathcal{L}_S is defined as the Binary Cross Entropy (BCE) and that the **ADAM** optimizer [Kingma and Ba, 2017] was used with a batch size of 50.

Concerning the validation step, the figure of merit we selected to report the validation performance is the median of the maximum accuracy. More precisely, for a given measurement point, in each run the maximum value of the accuracy is read over all epochs, then the median value is calculated

over the 299 maxima. The raw maximum accuracy has not been retained as we have considered it would have been an over-optimistic metric.

At the highest level, a grid search was conducted to find the best pairs of parameters (λ, σ) , for each $C/N0$ ratio and each N_{SUP} listed herebefore. The grid was built with $\lambda \in \{1, 10, 100, 1000\}$ and $\sigma \in \{0.01, 0.05, 0.1, 0.2, 0.5, 1.0, 2.0, 10.0\}$.

The implementation of the test bench used to build the data sets described in section 4.2 as well as to apply the experimental methodology detailed in this section is again freely available in the same repository which hosts the code of the CNN [Blais et al., 2025a].

5 Results and discussion

This section presents and discusses the outcomes of our experiments. To set a reference for SSL, the performance of fully supervised learning is first established. Then, the results for SSL are exposed in comparison to the reference. The results for the pairs of parameters (λ, σ) providing the largest gain over fully supervised learning are also detailed.

5.1 Performance of the fully supervised CNN

The median maximum accuracy achieved by the fully supervised CNN with respect to the number of training (labelled) samples N_{SUP} is displayed in Figure 3. The range of N_{SUP} is limited to $[25, 200]$ as below 25 learning turned out to be unreliable and above 200 the performance has reached a logarithmic growth region.

The effect of the $C/N0$ ratio on the network classification efficiency is clearly visible and coherent with the logic that for the same number of training samples the higher the signal to noise ratio is the higher the performance shall be. Besides, the three curves show two distinct areas. The first is a linearly increasing accuracy region for low N_{SUP} , which extends up to about 60 for $C/N0 = 43$ dBHz, 75 for $C/N0 = 40$ dBHz and 150 for $C/N0 = 37$ dBHz. One can observe that the lower the $C/N0$ is, the more extended this region is. In this region the effect of a small increase in the number of labelled samples greatly improves the results and even more so when the $C/N0$ ratio increases. The second region, for larger N_{SUP} , demonstrates a reduction in the performance improvement with N_{SUP} . Indeed, the behaviour is plainly logarithmic for $C/N0 = 43$ dBHz and $C/N0 = 40$ dBHz.

Figure 4 presents the quartiles for the reference results of Figure 3. The size of the quartiles does not exhibit the same trends as the median value. There is no significant shrinking of the quartiles with an increase in N_{SUP} nor in $C/N0$, except for few cases when $N_{\text{SUP}} \geq 150$ and $C/N0 \geq 40$ dBHz.

In light of Figure 3, the rest of the study has focused on $N_{\text{SUP}} \leq 75$ as above 75 the performance of the fully supervised CNN is already so high that the margins for improvement has seemed relatively weak.

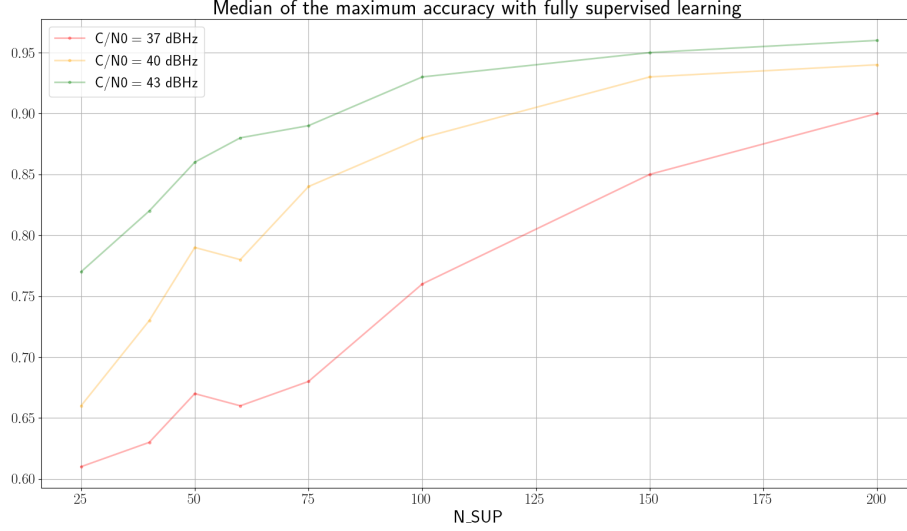


Figure 3: Median maximum accuracy for the fully supervised reference cases.

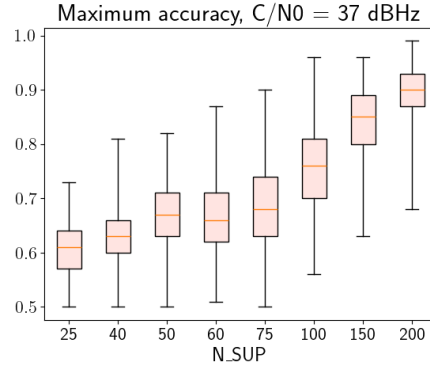
5.2 Performance of SSL and comparison with fully supervised learning

Figure 5 shows the best results obtained with the SSL CNN (bold curves) and recalls the performance of the fully supervised CNN (thin curves) as well. The pairs of parameters which have enabled the SSL network to achieve each particular score are also printed under the corresponding point of the curve.

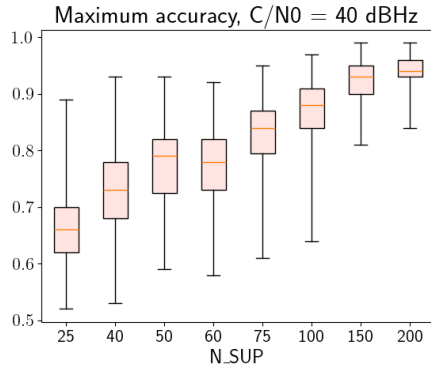
Except for $N_{\text{SUP}} = 25$ in combination with $C/N0 = 37$ dBHz and $N_{\text{SUP}} = 50$ in combination with $C/N0 = 40$ dBHz and 37 dBHz, there always exists at least one pair of parameters (λ, σ) which allows SSL to outperform fully supervised learning. The gain in median maximum accuracy can reach 5 % in the specific case of $N_{\text{SUP}} = 75$ for $C/N0 = 37$ dBHz and is never less than 1 % apart from the cases listed before. More precisely, on a total of 15 measurement points, 1 shows a loss of 2 % in performance, 2 a loss of 1 %, 4 a gain of 1 %, 2 a gain of 2 %, 4 a gain of 3 %, 1 a gain of 4 % and 1 a gain of 5 %. The balance is clearly in favour of SSL. Indeed, Figure 5 validates the relevance of our approach by showing that the introduction of unlabelled data improves the general learning performance of our model.

However, one can notice that no clear rule could be established to predetermine the pair(s) of parameters (λ, σ) which would bring the best result in any given conditions set by N_{SUP} and $C/N0$.

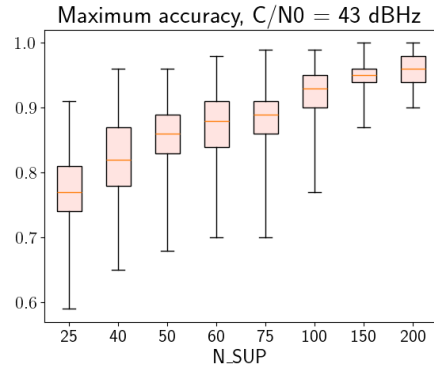
Figures 6, 7 and 8 detail the quartiles for the best results of Figure 5. For each plot the $C/N0$ ratio, N_{SUP} and λ are set and the quartiles of the maximum accuracy are plotted for the different values of σ . More specifically, these figures depict the following cases,



(a) $C/N_0 = 37$ dBHz.



(b) $C/N_0 = 40$ dBHz.



(c) $C/N_0 = 43$ dBHz.

Figure 4: Quartiles of the maximum accuracy for the fully supervised reference cases.

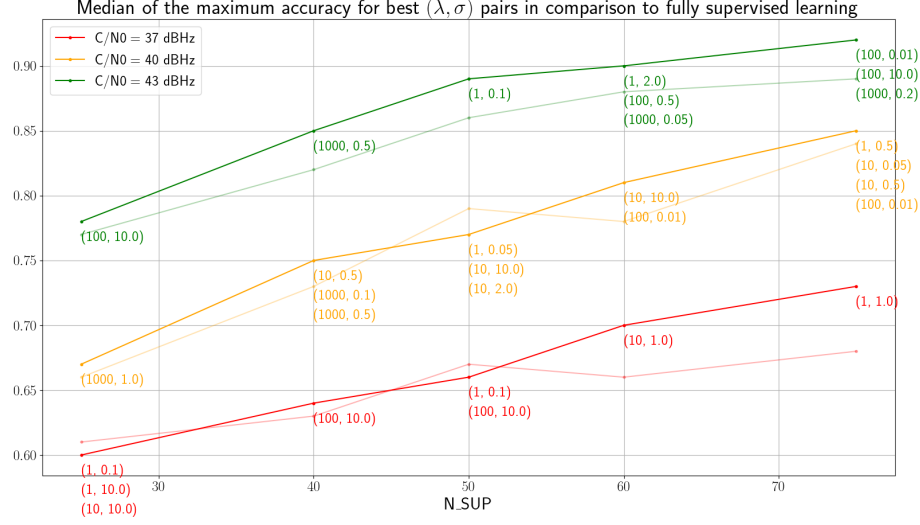


Figure 5: Median maximum accuracy for the SSL best pairs of parameters (λ, σ) and comparison with fully supervised learning. Bold curves represent the SSL results and the thin curves are for the fully supervised learning from Figure 3.

- Figure 6 for 37 dBHz: a gain of 5 % for $N_{\text{SUP}} = 75$ with $(\lambda, \sigma) = (1, 1.0)$,
- Figure 7 for 40 dBHz: a gain of 3 % for $N_{\text{SUP}} = 60$ in
 - Sub-figure (a) with $(\lambda, \sigma) = (10, 10)$
 - Sub-figure (b) with $(\lambda, \sigma) = (100, 0.01)$.
- Figure 8 for 43 dBHz: a gain of 3 % in
 - Sub-figure (a) for $N_{\text{SUP}} = 40$ with $(\lambda, \sigma) = (1000, 0.5)$,
 - Sub-figure (b) for $N_{\text{SUP}} = 50$ with $(\lambda, \sigma) = (1, 0.1)$,
 - Sub-figure (c) for $N_{\text{SUP}} = 75$ with $(\lambda, \sigma) = (100, 0.01)$ and $(100, 10.0)$,
 - Sub-figure (d) for $N_{\text{SUP}} = 75$ also with $(\lambda, \sigma) = (1000, 0.2)$.

The quartile plots for the other values of N_{SUP} , $C/N0$ and λ are available in the code repository already mentioned.

In each plot the quartiles of the reference case corresponding to the values of $C/N0$ and N_{SUP} are indicated by horizontal grey dashed lines.

Exactly as discussed in section 5.1 no significant variation in the quartile size arises from these plots as a function of the number of labelled samples N_{SUP} or depending on the $C/N0$ ratio. There is one exception, though, when $N_{\text{SUP}} = 25$ for the three values of $C/N0$ the performance of SSL is nearly every time significantly lower than for fully supervised learning. Figure 10 which can be found in Appendix B illustrates this observation. It could indicate that $N_{\text{SUP}} = 25$ labelled samples are too

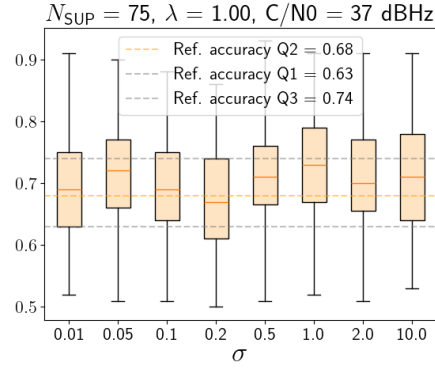


Figure 6: Quartiles of the maximum accuracy for $C/N0 = 37 \text{ dBHz}$, $N_{\text{SUP}} = 75$.

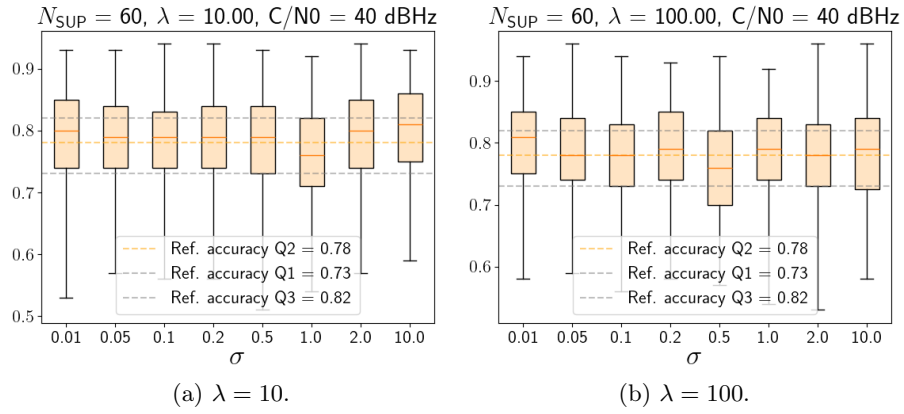


Figure 7: Quartiles of the maximum accuracy for $C/N0 = 40 \text{ dBHz}$, $N_{\text{SUP}} = 60$.

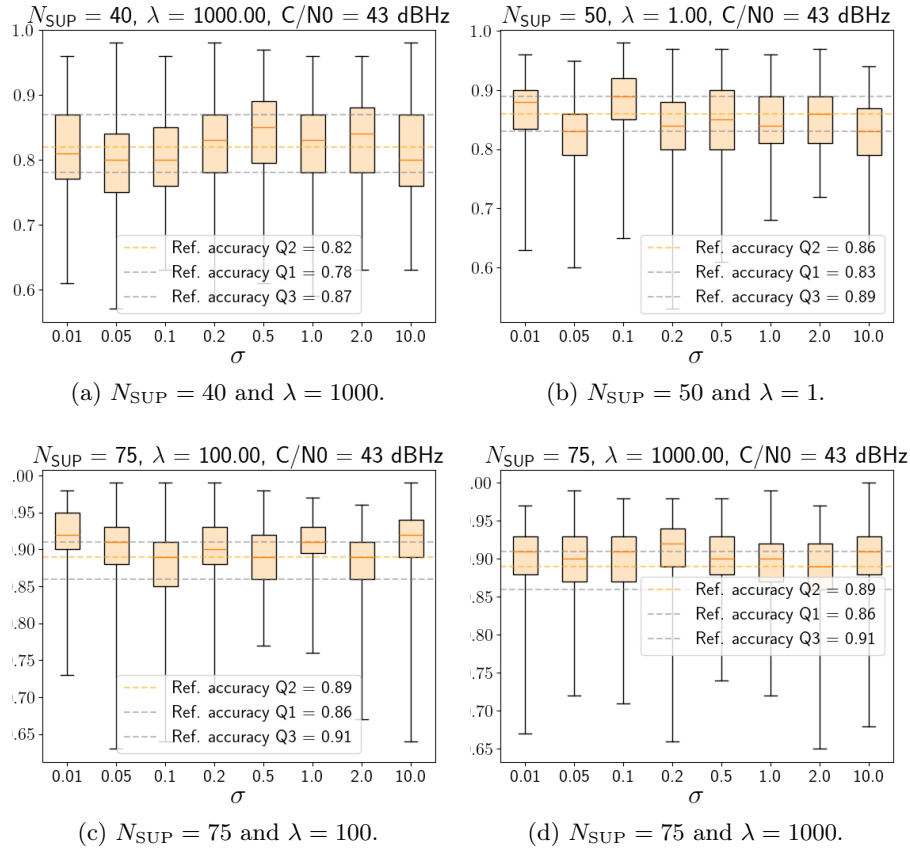


Figure 8: Quartiles of the maximum accuracy for $C/N0 = 43$ dBHz.

scarce for the network to learn accurately the manifold of the data. On another note, the comparison with the quartiles of the reference cases shows that they are similar in size indicating that the introduction of unlabelled samples, even in large number as for $N_{\text{SUP}} = 40$ with then $N_{\text{UNSUP}} = 160$, does not degrade the reliability of the classification statistics.

6 Conclusions

In this research work, we have proposed a semi-supervised classification method for images in situations where labelled data are scarce. The use of the Wasserstein distance as a similarity metric between image samples has enabled the graph-based transductive label propagation in the proposed CNN architecture. Furthermore, the study has demonstrated its efficiency on a real-life GNSS application. The results show that for various receiving conditions a gain in accuracy of up to 5 % can be achieved. This emphasizes the existence of some form of regularity in the GNSS data which can be exploited. We believe that it is also the case in many practical applications, accuracy results can be improved by introducing unlabelled samples in the learning process. This advocates also for the use of such techniques to reduce the generally expensive labelling procedure of *ground truth* data. However, so far no clear rule has been found to select the optimum values for the hyperparameters involved in the method and further investigation in this direction should be conducted.

References

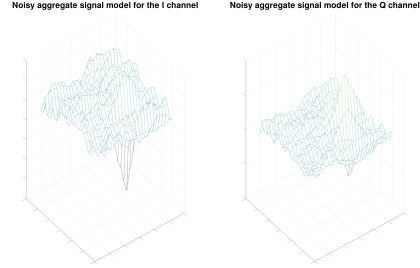
- [Arjovsky et al., 2017] Arjovsky, M., Chintala, S., and Bottou, L. (2017). Wasserstein generative adversarial networks. In Precup, D. and Teh, Y. W., editors, *Proceedings of the 34th International Conference on Machine Learning*, volume 70 of *Proceedings of Machine Learning Research*, pages 214–223. PMLR.
- [Belkin and Niyogi, 2003] Belkin, M. and Niyogi, P. (2003). Laplacian eigenmaps for dimensionality reduction and data representation. *Neural Computation*, 15(6):1373–1396.
- [Blais et al., 2022] Blais, A., Couellan, N., and Munin, E. (2022). A novel image representation of GNSS correlation for deep learning multipath detection. *Array*, 14:100167.
- [Blais et al., 2025a] Blais, A., Couellan, N., and Munin, E. (2025a). GNSS multi-path detection with SSL.
- [Blais et al., 2025b] Blais, A., Munin, E., and Couellan, N. (2025b). A synthetic GNSS correlator output generator.
- [Blum and Mitchell, 1998] Blum, A. and Mitchell, T. (1998). Combining labeled and unlabeled data with co-training. In *Proceedings of the Eleventh Annual Conference on Computational Learning Theory*, COLT’ 98, page 92–100, New York, NY, USA. Association for Computing Machinery.

- [Chapelle et al., 2006] Chapelle, O., Schölkopf, B., and Zien, A. (2006). *Semi-Supervised Learning*. MIT Press.
- [Chen et al., 2024] Chen, Y., Mancini, M., Zhu, X., and Akata, Z. (2024). Semi-supervised and unsupervised deep visual learning: A survey. *IEEE Transactions on Pattern Analysis and Machine Intelligence*, 46(3):1327–1347.
- [Cheng et al., 2020] Cheng, C., Zhou, B., Ma, G., Wu, D., and Yuan, Y. (2020). Wasserstein distance based deep adversarial transfer learning for intelligent fault diagnosis with unlabeled or insufficient labeled data. *Neurocomputing*, 409:35–45.
- [Engelen and Hoos, 2019] Engelen, J. E. V. and Hoos, H. H. (2019). A survey on semi-supervised learning. *Machine Learning*, 109:373 – 440.
- [Flamary et al., 2024] Flamary, R., Vincent-Cuaz, C., Courty, N., Gramfort, A., Kachaiev, O., Quang Tran, H., David, L., Bonet, C., Cassereau, N., Gnassounou, T., Tanguy, E., Delon, J., Collas, A., Mazelet, S., Chapel, L., Kerdoncuff, T., Yu, X., Feickert, M., Krzakala, P., Liu, T., and Fernandes Montesuma, E. (2024). Pot python optimal transport (version 0.9.5).
- [Friesecke, 2025] Friesecke, G. (2025). *Optimal transport : a comprehensive introduction to modeling, analysis, simulation, applications*. Other titles in applied mathematics ; 199. Society for Industrial and Applied Mathematics, Philadelphia, PA.
- [González et al., 2024] González, T., Blais, A., Couëllan, N., and Ruiz, C. (2024). Distributional loss for convolutional neural network regression and application to parameter estimation in satellite navigation signals. *Expert Systems with Applications*, 255:124682.
- [He et al., 2016] He, K., Zhang, X., Ren, S., and Sun, J. (2016). Deep residual learning for image recognition. In *2016 IEEE Conference on Computer Vision and Pattern Recognition (CVPR)*, pages 770–778.
- [Huang et al., 2018] Huang, G., Liu, Z., van der Maaten, L., and Weinberger, K. Q. (2018). Densely connected convolutional networks.
- [Kingma and Ba, 2017] Kingma, D. P. and Ba, J. (2017). Adam: A method for stochastic optimization.
- [LeNail, 2019] LeNail, A. (2019). NN-SVG: Publication-ready neural network architecture schematics. *Journal of Open Source Software*, 4(33):747.
- [Paszke et al., 2019] Paszke, A., Gross, S., Massa, F., Lerer, A., Bradbury, J., Chanan, G., Killeen, T., Lin, Z., Gimelshein, N., Antiga, L., Desmaison, A., Köpf, A., Yang, E., DeVito, Z., Raison, M., Tejani, A., Chilamkurthy, S., Steiner, B., Fang, L., Bai, J., and Chintala, S. (2019). Pytorch: an imperative style, high-performance deep learning library. In *Proceedings of the 33rd International Conference on Neural Information Processing Systems*, Red Hook, NY, USA. Curran Associates Inc.
- [Peyré and Cuturi, 2019] Peyré, G. and Cuturi, M. (2019). Computational optimal transport: With applications to data science. *Foundations and Trends® in Machine Learning*, 11(5-6):355–607.

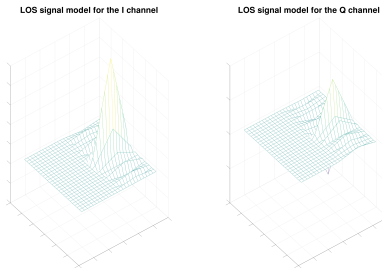
- [Rubner et al., 2000] Rubner, Y., Tomasi, C., and Guibas, L. (2000). The earth mover’s distance as a metric for image retrieval. *International Journal of Computer Vision*, 40:99–121.
- [Simonyan and Zisserman, 2015] Simonyan, K. and Zisserman, A. (2015). Very deep convolutional networks for large-scale image recognition.
- [Szegedy et al., 2016] Szegedy, C., Vanhoucke, V., Ioffe, S., Shlens, J., and Wojna, Z. (2016). Rethinking the inception architecture for computer vision. In *2016 IEEE Conference on Computer Vision and Pattern Recognition (CVPR)*, pages 2818–2826.
- [Weston et al., 2012] Weston, J., Ratle, F., Mobahi, H., and Collobert, R. (2012). Deep learning via semi-supervised embedding. In Montavon, G., Orr, G. B., and Müller, K.-R., editors, *Neural Networks: Tricks of the Trade: Second Edition*, pages 639–655, Berlin, Heidelberg. Springer Berlin Heidelberg.
- [Wright and Recht, 2022] Wright, S. J. and Recht, B. (2022). *Optimization for Data Analysis*. Cambridge University Press.
- [Xu et al., 2013] Xu, C., Tao, D., and Xu, C. (2013). A survey on multi-view learning. *CoRR*, abs/1304.5634.
- [Zhu, 2008] Zhu, X. (2008). Semi-supervised learning literature survey. Technical Report 1530, Computer Sciences, University of Wisconsin-Madison.

A I and Q images represented in 3-D

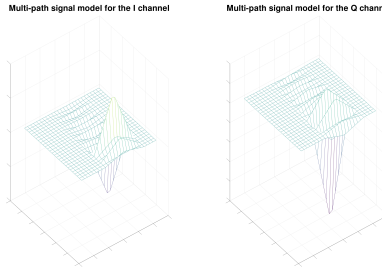
B Quartile plots for $N_{\text{SUP}} = 25$



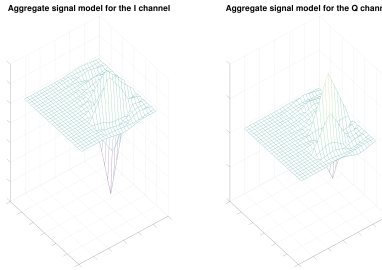
(a) Full image



(b) Direct signal model

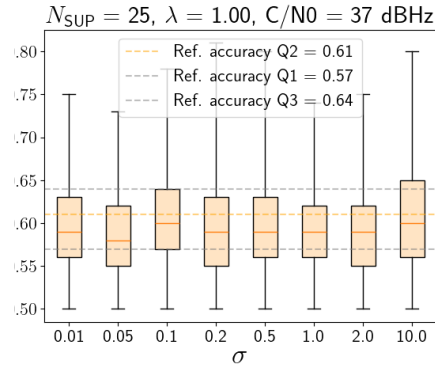


(c) Multi-path signal model

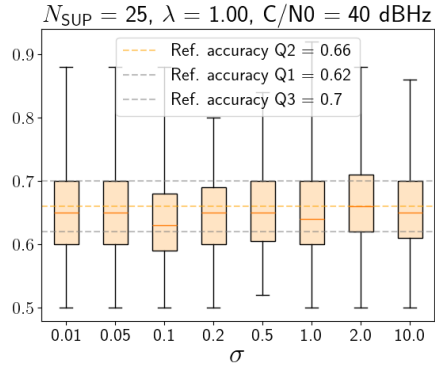


(d) Aggregate signal model

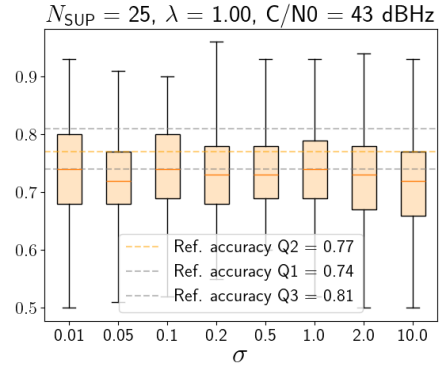
Figure 9: The same pairs of I and Q images as in Figure 1 represented in 3-D.



(a) $C/N0 = 37 \text{ dBHz}$.



(b) $C/N0 = 40 \text{ dBHz}$.



(c) $C/N0 = 43 \text{ dBHz}$.

Figure 10: Quartiles of the maximum accuracy for $N_{\text{SUP}} = 25$.